

A Scanning and Sampling Scheme for Computationally Efficient Algorithms of Computer Tomography

KEVIN D. DONOHUE, MEMBER, IEEE, AND JAFAR SANIIE, MEMBER, IEEE

Abstract—This paper presents a scanning and sampling scheme for computerized tomography that reduces the number of required interpolations in the reconstruction algorithm. Hence, the computational load associated with interpolation is also reduced. For the case where no restrictions are placed on the sampling rates of the scanner, a set of projection angles along with their corresponding sampling rates are derived such that no interpolation is required to calculate the final image points for the display grid. From this result a reduced interpolation scheme is developed for the case when upper and lower bounds exist on the sampling rates. A discussion is presented on the choice of an optimal set of projection angles that will maintain an image quality comparable to a sampling scheme of regular measurement geometry, while minimizing the computational load. The Cartesian-grid scanning and sampling (CGSS) scheme developed here is compared to a sampling scheme of regular measurement geometry through a computer simulation. The results demonstrate that for higher sampling rates and images of limited pixel dimension, the CGSS scheme can reduce the computational load of the reconstruction process and maintain comparable image quality.

I. INTRODUCTION

THE field of computerized tomography (CT) has generated much interest in reconstructing two-dimensional images from their sampled projections. This imaging process can be thought of in three stages. First is the data acquisition stage, which determines how the object will be scanned and exactly what samples will be taken. The second stage is the reconstruction algorithm that processes these samples to obtain image points. Finally, the reconstructed image must be displayed. This is usually done on a Cartesian grid. For data acquisition, the two basic projections are the parallel beam and the fan beam [1]. For either type of projection, the actual position of the detectors will determine the arrangement of samples in the Fourier domain. The reconstruction algorithm must be adapted to accept the particular set of samples determined by the scanning and sampling geometry [2]–

[6]. In the last stage, the algorithm must take the processed samples and perform interpolation to estimate the value of the discrete points on the Cartesian grid.

Given the general configuration for parallel- or fan-beam projections, different sampling schemes can be created by variations of the projection angles and sampling rates on each projection. In a typical parallel-beam scanner, an array of evenly spaced detectors positioned along a straight line (projection axis) measures the attenuation of a beam perpendicular to the detector array, which has traversed through the object (Fig. 1). This is done for every evenly spaced position along the projection axis. Then the whole axis is rotated about the center of the object by a fixed angular increment and the measurements are repeated. This type of geometry is referred to as a polar raster because the Fourier space in this case is sampled in an arrangement of concentric circles. A variation on this geometry was developed in previous work [7] to find a set of sampling rates that yields concentric squares in the sampled Fourier space (thus referred to as a concentric squares raster). This simplified the interpolation in the frequency domain to prepare the samples for a direct Fourier inversion. The technique not only reduced calculations, but also improved the image quality over that of the polar raster. Another scan and sample geometry was proposed for backprojection algorithms, which uses variable scanning steps coupled with a sampling rate that varies from scan to scan to eliminate interpolation from the reconstruction algorithm. This technique resulted in a reduction in the computational load for image reconstruction [8].

This paper presents a derivation of the set of special projection angles with corresponding sampling rates for parallel-beam projections that causes the reconstruction algorithm to calculate points that directly contribute to the image. The sampling scheme is derived from the geometry of the Cartesian grid so that the samples fed into the algorithm contain more information about the points of interest than the samples that must be interpolated for the display. The application of this scan and sample geometry to the filtered-backprojection algorithm is presented in the next section. A complete set of projection angles along with their corresponding sampling rates, which yield interpolation-free results, is derived for this algorithm. In

Manuscript received August 1, 1986; revised June 16, 1988. The work of the first author was supported by a fellowship from the American Electronics Association, while the author was in the Department of Electrical and Computer Engineering at the Illinois Institute of Technology.

K. D. Donohue was with the Department of Electrical and Computer Engineering, Illinois Institute of Technology, Chicago, IL. He is now with the Department of Electrical and Computer Engineering, Drexel University, Philadelphia, PA 19104.

J. Saniie is with the Department of Electrical and Computer Engineering, Illinois Institute of Technology, Chicago, IL 60616.

IEEE Log Number 8825664.

0096-3518/89/0300-0402\$01.00 © 1989 IEEE

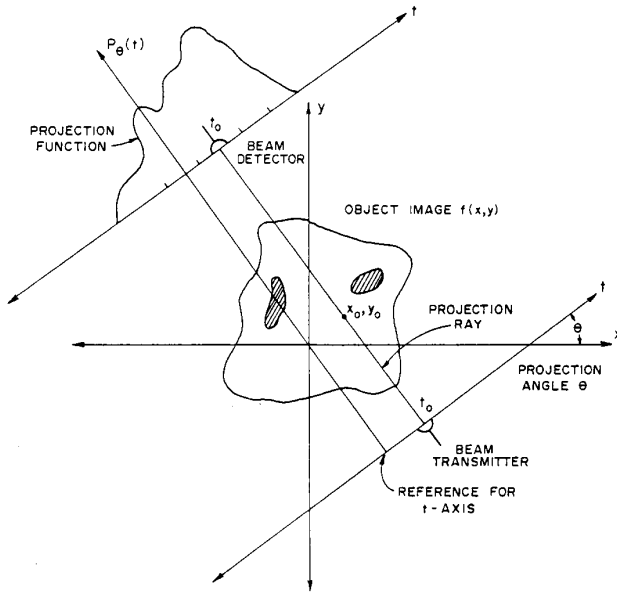


Fig. 1. Typical arrangement for a parallel-beam projection measurement. The function $P_\theta(t)$ represents the measurement of attenuation for each projection ray emitted from the projection axis at position t .

Section III, the choice of an optimal set of angles, which minimize computational effort while maintaining comparable image quality, is discussed. Since some of the required sampling rates for a given projection may be very high, a procedure is developed to find the best set under the constraint of upper and lower bounds for the sampling rates. In these cases a limited amount of interpolation is required. Finally, the results of a computer simulation compare the Cartesian-grid scanning and sampling (CGSS) scheme to the polar raster of regular measurement geometry and conclusions are drawn.

II. DEVELOPMENT OF AN INTERPOLATION-FREE PROJECTION SET

The filtered-backprojection algorithm reconstructs a cross-sectional image of an object from its backprojection data. The cross-sectional image of an object can be reconstructed from its projections [1] by

$$f(x, y) = \int_0^\pi \int_{-\infty}^{+\infty} S_\theta(\nu) |\nu| e^{j2\pi\nu t} d\nu d\theta \quad (1)$$

where $f(x, y)$ is the reconstructed image in the x - y plane, and $S_\theta(\nu)$ is the Fourier transform of the projection, $P_\theta(t)$, taken at angle θ

$$S_\theta(\nu) = \int_{-\infty}^{+\infty} P_\theta(t) e^{-j2\pi\nu t} dt \quad (2)$$

where t represents the position along the projection axis corresponding to image points that intersect the path of the projection ray in the x - y plane (see Fig 1). For a given projection angle, θ , the image points are related to the

position t along the projection axis by

$$t = x \cos \theta + y \sin \theta. \quad (3)$$

Now let

$$Q_\theta(t) = \int_{-\infty}^{+\infty} S_\theta(\nu) |\nu| e^{j2\pi\nu t} d\nu \quad (4)$$

where $Q_\theta(t)$ is referred to as the filtered-backprojection. The substitution of (3) and (4) into (1) results in

$$f(x, y) = \int_0^\pi Q_\theta(x \cos \theta + y \sin \theta) d\theta. \quad (5)$$

Since there are a finite number of samples available, (5) must be expressed in discrete form. If the projections of the object are considered approximately band-limited to some frequency less than B , and N samples span each projection, then (2) is approximated by

$$S_\theta(\nu) \approx \frac{1}{2B} \sum_{k=-N/2}^{+N/2} P_\theta\left(\frac{k}{2B}\right) e^{-j2\pi\nu k/2B} \quad (6)$$

and an approximation for (4) can be written as

$$Q_\theta\left(\frac{k}{2B}\right) \approx \frac{2B}{N} \sum_{m=-N/2}^{N/2} S_\theta\left(m \frac{2B}{N}\right) \left| m \frac{2B}{N} \right| e^{j2\pi m k/N}. \quad (7)$$

Error is introduced in the samples of $Q_\theta(t)$ due to the band-limited approximation. Since the image is spatially finite, the spectral information in the frequency components that exceed twice the sampling frequency result in aliasing error. This error is distributed throughout the spectral domain. To reduce this error, the image can be sampled at a higher rate, which decreases the amount of spectral energy contributing to this error.

Since only a finite number of projections is processed, the integral of (5) can be approximated (rectangular formula) by

$$f(x, y) \approx \frac{\pi}{I_p} \sum_{i=1}^{I_p} Q_{\theta_i}(x \cos \theta_i + y \sin \theta_i) \quad (8)$$

where Q_{θ_i} is the filtered-backprojection at angle θ_i and I_p is the total number of projections. The error associated with the approximation of (8) is discussed in the next section and in Appendix A.

Now if the reconstructed image is to be displayed on a Cartesian grid, then only a finite number of points are of interest. For every reconstructed point (x_0, y_0) , a corresponding value of $Q_{\theta_i}(t_{0,i})$ must be found for all θ_i , where $t_{0,i}$ is related to x_0, y_0 , and θ_i by (3). In (7), if $k/2B \neq t_{0,i}$ for some integer k and projection angle θ_i , then interpolation is required to obtain that value of $Q_{\theta_i}(t_{0,i})$. With some forethought, projection angles and sampling rates can be chosen such that

$$t_{k,i} = k\tau_i = x_i \cos \theta_i + y_m \sin \theta_i \quad \text{for all integers } k \quad (9)$$

where $t_{k,i}$ represents a position along the projection axis where a discrete sample is taken, τ_i is the sampling period used for the i th projection, and (x_l, y_m) is a point of the x - y plane corresponding to positions on the Cartesian grid. If (9) holds for all x_l and y_m , there is no need to interpolate to obtain the required points along each projection, since all the projection rays will focus on the points of interest. This situation is illustrated in Fig. 2, which shows the paths of the projection rays over a Cartesian grid. Note that for the eight projections drawn, the sampling rate is chosen so that every pixel area of interest is included in a line integral from each projection. A set of θ_i 's and their corresponding sampling rates that satisfy (9) is derived in the following discussion.

Consider an image, $f(x, y)$, sampled on a Cartesian grid with integer coordinates l and m . If l and m are substituted into (8) for x and y ,

$$f_s(l, m) \approx \frac{\pi}{I_p} \sum_{i=1}^{I_p} Q_{\theta_i}(l \cos \theta_i + m \sin \theta_i). \quad (10)$$

From (3) it follows that the projection angle and the associated sampling period τ_i is needed such that an integer k can be found to satisfy

$$k\tau_i = l \cos \theta_i + m \sin \theta_i \quad \text{for all integers } l \text{ and } m. \quad (11)$$

In order for (11) to be satisfied for a given projection, all the points of the Cartesian display (l, m) must project to the t -axis such that they are all evenly spaced. This condition is always satisfied for a single column of pixel points (constant l), since a projection of a set of evenly spaced points is also evenly spaced (see Fig. 3). The actual sampling period, τ_c , for this column of constant l can be found by substituting in two consecutive points (in m) into (11) to obtain two equations. If both equations are subtracted, the result is

$$\tau_{c_i} = \sin \theta_i. \quad (12)$$

Note that any other set of equally spaced samples will also project all the image points of some column on to the t -axis as long as their intervals are related to the fundamental interval τ_{c_i} by

$$\tau_{(nc)_i} = \frac{\tau_{c_i}}{(nc)} \quad \text{for } nc = 1, 2, 3, \dots \quad (13)$$

In this case, nc will be the number of sampling periods between two adjacent image points of a single column of constant l . The set of all possible sampling periods for this case is given by

$$\left\{ \tau_{(nc)_i} \mid (nc)\tau_{(nc)_i} = \sin \theta_i \quad \text{for } nc = 1, 2, 3, \dots \right\}. \quad (14)$$

If (9) is to be satisfied for the whole Cartesian plane, then the set of sampling rates given in (14) must also project the image points of all other columns on to the projection axis. This can be satisfied if just one projection ray will

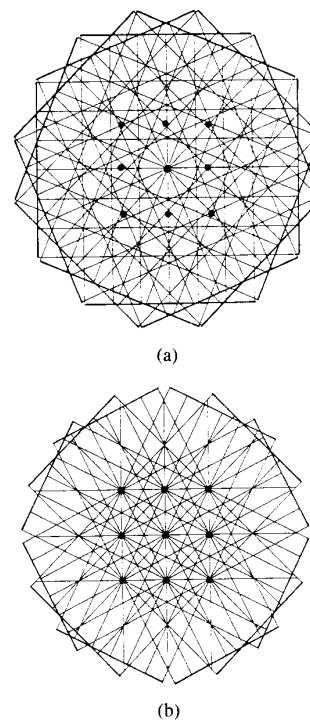


Fig. 2. (a) Projection rays for 8 projections of a polar raster scheme with regular measurement geometry superimposed on a 3 by 3 Cartesian grid. (b) Projection rays for 8 projections of the CGSS scheme superimposed on a 3 by 3 Cartesian grid.

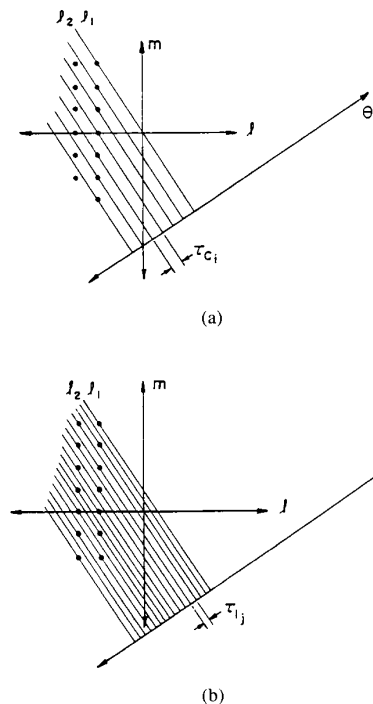


Fig. 3. (a) Sampling period τ_{c_i} projects an entire column of constant l on to the projection axis but it fails to project the adjacent column on to the axis. (b) Sampling period τ_{l_j} projects a column of constant l and its adjacent column on to the projection axis.

intersect a point in an adjacent column. Recall that the sampling rates given in (14) project any column of image points on to the projection axis. At this sampling rate, it is sufficient for one point in the adjacent column to intersect a projection ray to guarantee the intersection of all points in that column with the projection rays. The two-dimensional periodicity of the Cartesian grid also guarantees that the points in the following adjacent columns will intersect with the projection angles. Fig. 3(a) shows a case where a sampling rate will project one column on to the projection axis but not the adjacent column. Fig. 3(b) shows a case where the sampling rate projects both columns on to the projection axis.

Now to guarantee that all points in the Cartesian grid intersect the projection rays for a given sampling rate, consider a single row of constant m (see Fig. 4) and two consecutive points in that row. Since the coordinates of these points have a constant m and their l values differ by one, the two points can be substituted into (11) and the two equations can be subtracted to yield

$$\tau_{r_i} = \cos \theta_i. \quad (15)$$

The set of all possible sampling periods that projects this row on to the projection axis is given by

$$\left\{ \tau_{(nr)_i} \mid (nr)\tau_{(nr)_i} = \cos \theta_i \quad \text{for } nr = 1, 2, 3, \dots \right\}. \quad (16)$$

In this case, nr is the number of sampling periods between two points in a single row of constant m .

If a sampling rate exists that satisfies (16) and (14) simultaneously, it will also satisfy (9) for all x_j and y_m . Therefore, if (14) and (16) have a common sampling period ($\tau_i = \tau_{(nr)_i} = \tau_{(nc)_i}$), the division of the condition in (14) by that in (16) results in

$$\frac{nc}{nr} = \tan \theta_i. \quad (17)$$

The relationship in (17) now limits the set of projection angles to those angles whose slopes are rational numbers (since nc and nr are integers). The entire set of projection angles that satisfy the interpolation-free condition is given by

$$\left\{ \theta_i \mid \theta_i = \tan^{-1} \left(\frac{nc}{nr} \right) \quad \text{for all integers } nr \text{ and } nc \right\}. \quad (18)$$

For a given nc and nr , the corresponding sampling period for that projection can be obtained by squaring the sampling intervals of (14) and (16), adding them and solving for τ_i to yield

$$\tau_i = \frac{1}{\sqrt{(nr)^2 + (nc)^2}}. \quad (19)$$

If the displayed image is limited to the region $\{(l, m) \mid 0 \leq l \leq L, 0 \leq m < M\}$, then the number of samples for

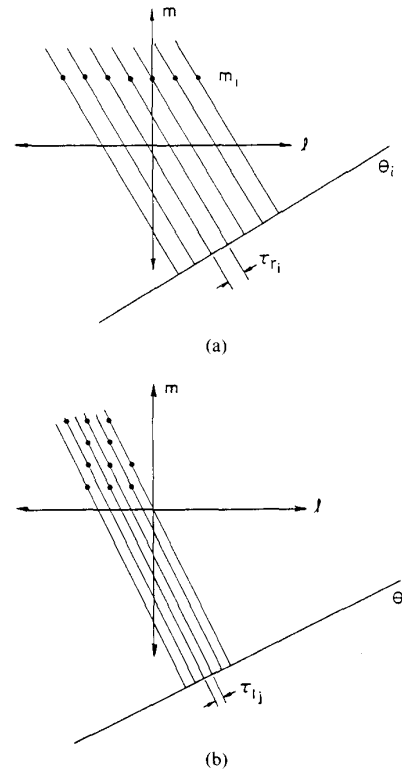


Fig. 4. (a) Sampling period τ_{r_i} projects a single row on to the projection axis. (b) Sampling period τ_{l_j} projects two adjacent columns on to the projection axis.

each projection can be derived by the relationships given in (14) and (16). Recall that nr represents the number of sampling periods between two points of consecutive m . Therefore, the row closest to the projection axis projects $nr(M - 1) + 1$ points on to the axis. A similar argument for the closest column to the projection axis yields $nr(L - 1) + 1$ points. Since there is only one sample that is common to both sets of image points and the particular row and column together span the area of interest relative to the projection axis, the total number of samples for each projection is given by

$$N = nr(M - 1) + nc(L - 1) + 1. \quad (20)$$

III. OPTIMAL SET OF PROJECTION ANGLES

Since any θ_i and τ_i satisfying (18) and (19) yields an interpolation-free set of samples, a set of θ_i 's must be found to minimize computational effort without any significant increase in the error of the reconstructed image. For the filtered-backprojection algorithm, some of the artifacts are due to the finite number of projections and the finite amount of samples on each projection [9]. If the projections are assumed to be approximately band-limited, a sampling rate can be chosen greater than twice the Nyquist rate. This rate can be used as a lower limit for the sampling rates. This constraint does not present any real problem for any of the projection angles since the

sampling rate can always be increased by integer multiples for a given θ_i .

Another source of artifacts in the reconstructed image is the calculation of the integral in (5) by the approximation in (8). This error will depend on the nature of the function $Q_\theta(t)$ for a single image point (x_0, y_0) as θ varies from 0 to π . To examine this error more closely, it would be helpful to modify the notation for $Q_\theta(t)$. Since $Q_\theta(t)$ is integrated over θ for a particular image point (x, y) , let this function be denoted by $Q_{x,y}(\theta)$. In the conventional polar raster scheme, $Q_{x,y}(\theta_i)$ is obtained from every projection by interpolation on each projection. The image point, $f(x, y)$, is then evaluated by (5). If $e_{LI}^{(i)}$ is the error due to linear interpolation from the i th projection and e_{RFM} is the error due to numeric integration by the rectangular formula using the midpoint on each angular interval, then the total error in the reconstructed image point is

$$e_{f(x,y)} = e_{RFM} + \frac{\pi}{I_p} \sum_{i=1}^{I_p} e_{LI}^{(i)}. \quad (21)$$

The error terms e_{LI} and e_{RFM} can be considered random variables. These random variables are described in Appendix A, where an analytical relationship is shown between the autocorrelation function of the filtered-backprojection data and the error.

The CGSS scheme will not generate the error represented by the linear interpolation terms in (21), but it will generate an error term due to the approximation of numeric integration different from e_{RFM} , since the midpoint of the intervals are not used. As shown in Appendix A, if a point corresponding to the average value of $Q_{x,y}(\theta)$ on each subinterval of integration is symmetrically distributed over the interval, the midpoint is the best choice to reduce the mean square error. Since for the CGSS scheme the midpoint cannot be chosen every time, the mean square error will typically be greater than the conventional polar raster error, e_{RFM} . Therefore, to reduce the error for the CGSS scheme, the set of θ_i 's should be chosen as close to the midpoint of the integration subintervals as possible.

In the choice of the optimal set of projection angles for the CGSS scheme, the cost of computational effort and image error must be assigned. A true optimum set would require the cost function for error and computation to be known. In this case, it is desired to minimize the computational effort while maintaining a comparable image quality. If the function $Q_{x,y}(\theta)$ is highly correlated within the angular sampling interval, the choice of a point in that interval for the evaluation of that function is not critical. Therefore, the freedom of the CGSS scheme to search for an optimal angle can be limited to half a sampling period (angular interval) either side of the midpoint. If it cannot be assumed that the function is sufficiently correlated in this interval, then a smaller interval about the midpoint must be used. This smaller interval can be chosen significantly higher than the Nyquist sampling period to guarantee a sufficiently high correlation in the interval.

In the case of the CGSS scheme, angles 0 to π can be broken into I_p uniform angular intervals and one projection angle within each interval can be chosen. This gives some flexibility to the choice of projection angles, but at the same time forces the error to be comparable to the sampling schemes that take projections at uniform intervals. If the sampling rates on each projection are such that the aliasing error is insignificant, then the mean square error in the CGSS scheme reconstruction will be less than the error of the conventional polar raster under the condition that

$$E \left\{ \left(e_{RFM} + \frac{\pi}{I_p} \sum_{i=1}^{I_p} e_{LI}^{(i)} \right)^2 \right\} \geq E \{ e_{RF}^2 \} \quad (22)$$

where e_{RF} is the error when the points of the CGSS scheme are used in numeric integration. Whether or not this condition is true depends on the autocorrelation or bandwidth of $Q_{x,y}(\theta)$ as described in Appendix A.

If the above restrictions are satisfied for the error criterion, the computational effort is now the major factor in governing the choice of an optimum set of projection angles for the CGSS scheme. The computational load has been reduced by eliminating the need for interpolation, but the computations performed by the fast Fourier transform (FFT) may increase due to the large amount of samples taken for some projection angles. Therefore, an optimal set of projection angles can be considered to be a set of angles such that one, and only one, angle lies within each of the I_p angular intervals, and within each interval the angle chosen minimizes the required number of samples.

The choice of these projection angles can be illustrated graphically (Fig. 5). From (19) and (21), the projection angles and sampling rates are shown to be functions of the integers nr and nc . Therefore, consider an nr - nc coordinate system as shown in Fig. 5. The sampling rates for any nr and nc can be expressed as

$$W_i(nr, nc) = \frac{1}{\tau_i} = \sqrt{nr^2 + nc^2} \quad (23)$$

where W_i is the sampling rate for the i th projection. Graphically, the minimum sampling rate can be represented by the nr - nc coordinate that is closest to the origin. The constraint of a lower bound, W_{min} , on all sampling rates can be chosen to limit the effect of aliasing on each projection. This new constraint requires that nr and nc satisfy

$$nr^2 + nc^2 \geq W_{min}^2 \quad (24)$$

which is represented by an area outside a circle of radius W_{min} . For a particular angular interval nr and nc must satisfy

$$\tan \left(\theta_{im} - \frac{a\pi}{2I_p} \right) \leq \frac{nc}{nr} < \tan \left(\theta_{im} + \frac{a\pi}{2I_p} \right) \quad (25)$$

where θ_{im} is the midpoint of the subinterval, and a is a parameter between 0 and 1 used to limit the interval

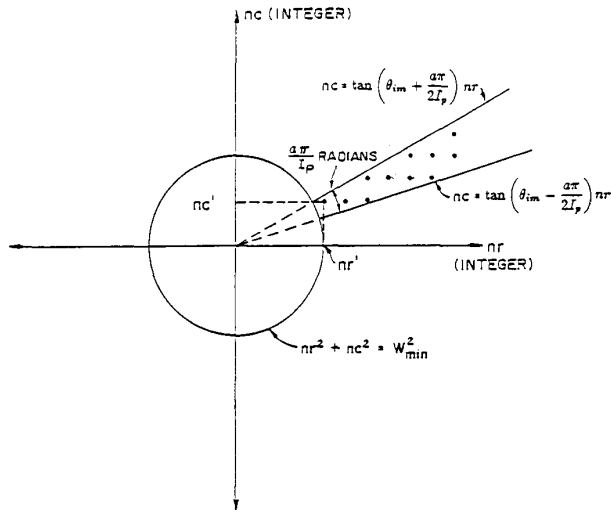


Fig. 5. Graphic representation of projection angles and corresponding sampling rates that generate an interpolation-free sampling scheme. For any integer coordinate point in the nr - nc plane, the projection angle it represents is given by $\theta = \tan^{-1}(nc/nr)$. The sampling rate for that point is $W = \sqrt{nr^2 + nc^2}$. The circle represents the minimum sampling rate that was chosen to limit the aliasing error of the projections, therefore, no sampling rate is chosen within this region. The two radial lines represent an angular interval of (π/I_p) that was chosen to ensure that the projections are taken as uniformly as possible around the object. In this case, the point (nr', nc') represents the projection angle with the minimum sampling rate in the given region.

around the midpoint. Equation (25) represents an area on the nr - nc plane, which is a sector bounded by two radial lines from the origin with slopes $\tan(\theta_{im} - a\pi/2I_p)$ and $\tan(\theta_{im} + a\pi/2I_p)$. Within the intersection of these areas, a search for a minimum sampling rate (integer coordinate point closest to origin) is carried out (Fig. 5). This search for an optimal set can be implemented numerically on a computer.

Another constraint that makes the sampling scheme more practical is an upper bound on the sampling rate W_{max} . This constraint may be determined by the scan and sample mechanism or the amount of sampling points that can be processed per projection. This constraint modifies the graph of the sampling rates on the nr - nc plane with an additional circle creating an annular region shown in Fig. 6. This additional constraint may define an area that does not include an integer coordinate point for some projection angle. In the regions where this is the case, interpolation is needed to estimate the value of the points used in the algorithm. For this situation, the sampling rate can be found by multiplying W_{min} and W_{max} by some increasing integer n until the region on the graph contains an integer coordinate point. Then instead of sampling at the rate required by (19), divide this rate by the integer n to obtain a lower rate that is within the original region. This new sampling rate now corresponds to every n th point that is actually needed, and the $n - 1$ points in between will have to be estimated by some interpolation scheme. In this situation, interpolation is necessary to obtain those inter-

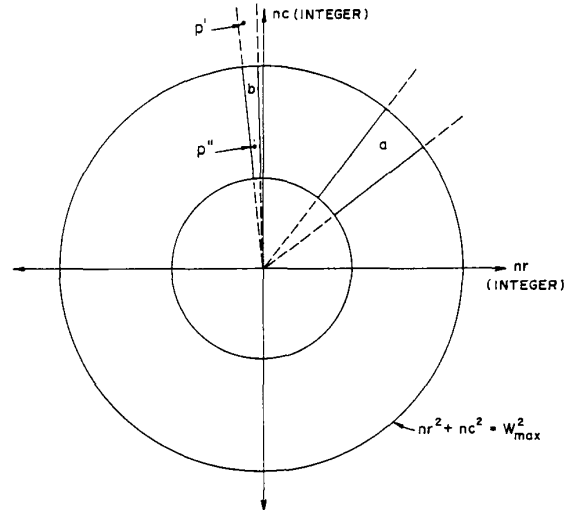


Fig. 6. Graphic illustration of the situation when an upper bound is imposed upon the sampling rates. Some regions may not be affected as in the case of region (a), but in other cases, as shown by region (b), an integer point may not exist. In this case, a point is found beyond the maximum sampling rate and is scaled down by an integer so that its value will fall in region (b). This is illustrated by the points p' and p'' . In this case, p'' is not an integer coordinate point and thus interpolation is required.

that the points in between the sampled points are known to be equally spaced and this permits computationally efficient interpolation.

If the CGSS scheme is modified by the above restriction and some interpolation is now necessary, the error for the reconstructed image point (due to interpolation) is given by

$$e_{f(x,y)} = e_{RF} + \frac{\pi}{I_p} \sum_{i=1}^{I_p} e_{LI}^{(i)}. \quad (26)$$

The above equation shows that the error will increase by the amount corresponding to the sum of linear interpolation errors. The summation of $e_{LI}^{(i)}$ terms in (26) is different from the corresponding summation in (21), in that the terms of the summation in (26) are zero for values of i where the particular i th projection did not require interpolation. In addition to this, for the projections that required interpolation, not all the points were created by interpolation and these points will also contribute a value of zero to the sum. Hence, when only a limited amount of interpolation is required for the CGSS scheme, the mean square error of the summation of error terms corresponding to linear interpolation in (26) is less than the corresponding expected values in (21), but the mean square error corresponding to numerical integration (e_{RFM}) in (21) is less than the corresponding mean square error (e_{RF}) in (26). This modified CGSS scheme will become advantageous when these errors will offset one another and comparable image quality can be obtained.

IV. SIMULATION RESULTS AND DISCUSSION

The CGSS scheme was compared to a polar raster with

struction using computer simulated data from the Shepp and Logan head phantom [10]. An analysis of the images has demonstrated that an image can successfully be reconstructed using the CGSS scheme with some improvements in efficiency.

Table I contains information about the head phantom used in this simulation. This particular phantom is used frequently in simulations for the evaluation of the performance of an algorithm. It is composed of 10 ellipses superimposed on a square background. The relative positions and sizes of these ellipses are given in Table I along with a drawing identifying the various ellipses and the densities of each region. The head phantom used here actually varies slightly from the one used by Shepp and Logan. The densities of the inner ellipses were increased over the typical Shepp and Logan head phantom so their details could be seen more clearly in the photographs of the display. In Figs. 7-10, each pixel of the 64 by 64 grid is magnified by a factor of four. Thresholding and scaling is used to further bring out the details of the inner ellipses. The equations used in generating the simulated backprojection data can be found in [1].

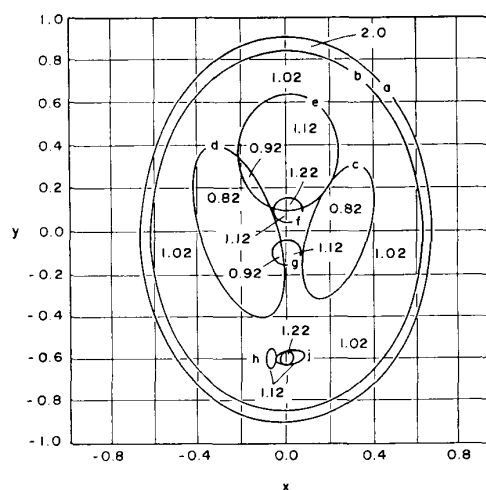
The reconstructions were performed by the filtered-backprojection algorithm using 64 projections taken over 180° . If more projections are required, the search interval for projection angles of the CGSS scheme decreases, further limiting the choice of efficient projection angles. The increased calculations due to this situation significantly limit the efficiency of the CGSS scheme when a larger number of projections are required.

The amount of calculations to obtain the filtered-backprojection were reduced by the use of an FFT that filtered the data in the frequency domain. Linear interpolation was used in the reconstruction algorithms where interpolation was required. No smoothing was used on the projection data and there was no modification of the filter $|v|$ [from (4)].

The filtered-backprojection algorithm was adapted to accept the data from the CGSS scheme. The particular projection angles and sampling periods used for this scheme are given in Table II. Only the angles between 0 and 45° are listed since the symmetry of the Cartesian grid along its diagonal allows the angles between 45 and 90° to be determined by inverting the slopes of the angles between 0 and 45° , and the angles between 90 and 180° are simply the negative inverses of the slopes of the angles between 0 and 90° . The information about the particular angles used for sampling was provided to the reconstruction algorithm so that it could process each set of projection samples and combine all the projections together to reconstruct the image. The projection angles of Table II were chosen to minimize the sampling rate within each angular interval of $(180/64)^\circ$. For each projection angle in Table II, the corresponding sampling periods were calculated for an interpolation-free condition. The number of samples for the modified CGSS scheme, under the constraint of different upper bounds, are also included in Table II.

TABLE I
RELATIVE POSITIONS, SIZES, AND ORIENTATIONS OF THE TEN ELLIPSES USED FOR SIMULATING THE PARALLEL-BEAM PROJECTIONS FOR THE RECONSTRUCTION ALGORITHMS. THE DENSITIES OF EACH REGION ARE INDICATED ON THE DIAGRAM BELOW

Ellipse	Coordinates of the Center	A Major Axis	B Minor Axis	α Rotation Angle
a	(0,0)	0.92	0.69	0
b	(0, -0.0184)	0.874	0.6624	0
c	(0.22, 0)	0.31	0.11	72°
d	(-0.22, 0)	0.41	0.16	108°
e	(0, 0.35)	0.25	0.21	0
f	(0, 0.1)	0.046	0.046	0
g	(0, -0.1)	0.046	0.046	0
h	(-0.08, -0.605)	0.046	0.046	0
i	(0, -0.605)	0.023	0.023	0
j	(0.06, -0.605)	0.046	0.023	90°



It should be noted from Table II that when no restrictions are applied to the sampling rates, the dynamic range for the sampling period is from 1 to 0.0712 units. This range may be difficult to attain for scanning systems. If this is the case, then it is necessary to apply the upper and lower bounds as indicated in Fig. 6. For example, if we choose an upper bound of 512 samples per projection and a lower bound of 128 samples per projection, the dynamic range for the sampling period would then be from 0.5 to 0.1424, which reduces the range by about a factor of 4. Further restrictions can be placed on the minimum and maximum sampling rates to accommodate other possible limitations of the system.

The amount of real multiplications for the main components of the algorithm are given in Table III along with the amount of samples taken. The tabulated samples are only those samples whose projection rays pass through the 64 by 64 grid area. For the regular measurement geometry, not all samples on the projection pass through the 64 by 64 grid area of interest, so these samples were excluded from the count. The average sampling period is also included for comparing resolution capabilities. The amount of real multiplications for the FFT routines is

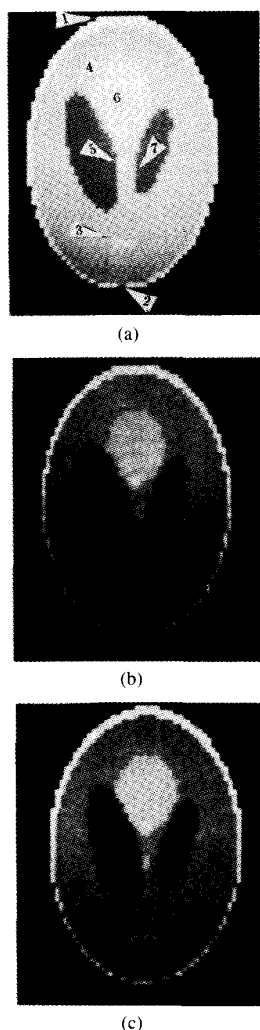


Fig. 7. Head phantom from Table I sampled on a 64 by 64 pixel Cartesian grid. Refer to Table II for the specific angles and sampling rates used in the reconstructions based on the CGSS geometry. (a) The actual head phantom displayed on a Cartesian grid. (b) Head phantom reconstructed from the CGSS scheme samples with no limits on the sampling rates. (c) Head phantom reconstructed from 1024 samples per projection using the polar raster scheme.

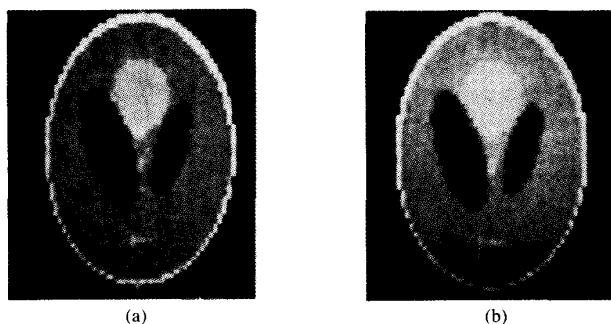


Fig. 8. Reconstructed images continued from Fig. 7. (a) Head phantom reconstructed from the samples of the CGSS scheme with an upper bound of 512 samples per projection. (b) Head phantom reconstructed from 512 samples per projection using the polar raster scheme.

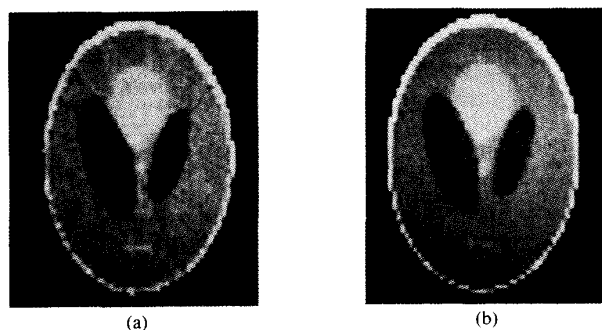


Fig. 9. Reconstructed images continued from Fig. 7. (a) Head phantom reconstructed from the samples of the CGSS scheme with an upper bound of 256 samples per projection. (b) Head phantom reconstructed from 256 samples per projection using the polar raster scheme.

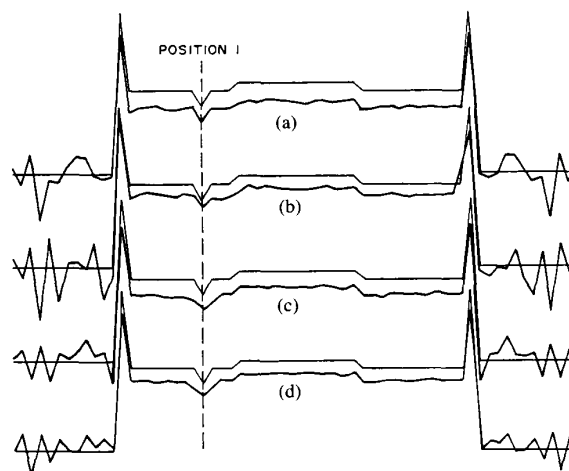


Fig. 10. Profiles of the reconstructed head phantom images (dark line) and the actual profile (light line) for row 20 of the images. The following schemes were used: (a) CGSS scheme with no sampling bounds; (b) CGSS scheme with an upper bound of 512 samples per projection; (c) polar raster scheme with 1024 samples per projection; (d) polar raster scheme with 512 samples per projection.

computed by the formula $16N \log_2 2N$, where N is the number of data points for each projection and the factor of $2N$ represents the number of points after padding zeros to prevent aperiodic interference. The filter requires a complex multiplication for every point transformed into the frequency domain. The linear interpolation requires two multiplications per image point (64^2) for every projection (64). Also included in this number are the two multiplications ($x \cos \theta + y \sin \theta$) required to locate each point on the projection axis.

The required number of samples is linearly dependent on the image pixel dimension (20), provided the number of projections remain constant. If the pixel dimension of the image were increased, it would significantly increase the required number of samples for the CGSS reconstruction. When the number of samples reach an impractical value, restrictions on the sampling rates can again be applied to limit the number of real samples. In these cases, interpolation would then be necessary and there would be

TABLE II
PROJECTION ANGLES CHOSEN FROM THE CGSS SCHEME USED TO SAMPLE THE SIMULATED HEAD PHANTOM AND RECONSTRUCT ON A 64 BY 64 CARTESIAN GRID. THE SLOPE OF EACH ANGLE AND ITS CORRESPONDING SAMPLING INTERVAL FOR AN INTERPOLATION-FREE SET OF DATA ARE GIVEN WITH THE TOTAL NUMBER OF SAMPLES PER PROJECTION IN THE LAST THREE COLUMNS. THE LAST TWO COLUMNS REPRESENT THE SAMPLING RATE UNDER THE CONSTRAINT OF AN UPPER BOUND. ONLY THE ANGLES FROM 0 TO 45 DEGREES ARE LISTED

Angle (θ_i)	Slope ($\frac{nc}{nr}$)	Sampling Interval (τ_i)	Number of Samples Required Under the Constraints of:		
			None	512 Maximum	256 Maximum
0.00°	$\frac{0}{1}$	1.	64	64	64
4.09°	$\frac{1}{14}$.0712	961	480	240
6.34°	$\frac{1}{9}$.1104	641	320	213
9.46°	$\frac{1}{6}$.1644	449	449	224
11.31°	$\frac{1}{5}$.1961	385	385	192
14.04°	$\frac{1}{4}$.2425	321	321	160
15.95°	$\frac{1}{3}$.1574	577	288	192
18.44°	$\frac{1}{3}$.3162	257	257	128
21.80°	$\frac{2}{3}$.1857	449	449	224
26.57°	$\frac{1}{2}$.4472	193	193	193
29.05°	$\frac{3}{5}$.0971	897	448	224
30.96°	$\frac{3}{5}$.1715	513	256	128
33.69°	$\frac{2}{3}$.2774	321	321	160
36.37°	$\frac{3}{4}$.2000	449	449	224
38.66°	$\frac{4}{5}$.1562	577	288	192
41.19°	$\frac{7}{8}$.0941	961	480	240
45.00°	$\frac{1}{1}$.7071	129	129	129

TABLE III
NUMBER OF SAMPLES AND REAL MULTIPLICATIONS REQUIRED BY THE FILTERED-BACKPROJECTION ALGORITHM FOR CASES WHERE THE SAMPLING WAS PERFORMED BY THE POLAR RASTER SCHEME OF REGULAR MEASUREMENT GEOMETRY AND THE CGSS SCHEME. THE AVERAGE SAMPLING PERIOD IS ALSO GIVEN

Samples per Projection	Number of Total Samples	Sampling Interval	Number of Real Multiplications		
			FFT Routines	Filter	Interpolation
1024	52,021	.0883	11,534,336	525,228	1,048,576
512	26,011	.1768	5,242,880	262,144	1,048,576
256	13,462	.3535	2,359,296	131,072	1,048,576

Limit on Samples per Projection	Number of Total Samples	Sampling Interval (Average)	Number of Real Multiplications		
			FFT Routines	Filter	Interpolation
None	32,190	.1597	7,575,552	357,376	0
512	21,922	.2345	4,642,816	234,496	20,480
256	12,122	.4240	2,128,896	119,808	40,088

an increase in image reconstruction error and computational effort. But this problem would also affect the conventional polar raster scheme. If the number of samples were limited and the image pixel dimension increased, there would be greater distances between the samples and the image pixels of the reconstruction. This would increase interpolation error in either case, but particularly for the modified CGSS scheme, a significant increase in the required amount of interpolation would increase the image error and computational effort, such that the advantage of the CGSS scheme over the regular measurement geometry would become insignificant. Therefore, this situation limits the CGSS scheme to reconstructions on smaller Cartesian grids.

Fig. 7(a) displays the actual image that is to be reconstructed. The arrows on the picture are numbered to indicate the features that will be points of interest in the discussion. Fig. 7(b) and (c) compares the reconstruction of the image using the CGSS scheme (7b) and the polar raster with regular measurement geometry 7(c). The amount of data points per projection is limited to 1024 for both schemes. For the CGSS scheme, only 28 projections contained the full 1024 points (after padding with zeros), while for the polar raster all 64 projections contained the full 1024 points. Note in Table III that the image of Fig. 7(b) was reconstructed with only 62 percent of the samples and 60 percent of the real multiplications that were used in the polar raster reconstruction of Fig. 7(c). The most apparent improvements in the image quality are noticed at the boundaries (features 1 and 2). The effects of the polar raster scanning [Fig. 2(b)] and linear interpolation can be seen clearly at these points in Fig. 7(c). Also note the boundaries around the inner ellipses are reproduced more accurately with the CGSS scheme as indicated by feature 4. The three smaller ellipses pointed out as feature 3 are also reproduced more accurately, and size is preserved better (even though the sampling rate for the polar raster is on average about 1.8 times greater than the CGSS scheme).

Finally, features 5, 6, and 7 display areas where the polar raster performed better. The two small ellipses (features 5 and 6) and the boundary (feature 7) are more definite in the polar raster reconstruction. A reason for this could be the concentration of projection rays in the center of the image for the conventional polar raster. If Fig. 2(a) and (b) are compared, it is noted that each image pixel for the CGSS scheme is intersected by the same amount of projection rays independent of their position in the Cartesian grid. In the regular measurement geometry, where the projections are rotated about the center of the image, this area has a high concentration of projection rays. Another reason for this degradation in the case of the CGSS scheme could be the absence of any type of signal processing to reduce the effect of noise and artifacts introduced by the algorithm [9]. The linear interpolation provides the algorithm with the benefit of signal averag-

ing (of two adjacent points) that eliminates some of the degradation introduced by the limitations of the algorithm. An averaging window may improve the results of the CGSS scheme, but it will also introduce smearing. An alternative to averaging could be the median filter [11], which is known to preserve edges.

In Figs. 8 and 9, upper bounds are applied to the sampling rates of the CGSS scheme. This modified CGSS scheme now requires interpolation (Table III). Fig. 8(a) (CGSS scheme) displays a reasonable image quality and is still superior to Fig. 8(b) with features 1, 3, and 4, but some degradation along the boundaries is indicated by feature 2. The reconstruction in Fig. 8(a) was performed with only 67 percent of the samples and 88 percent of the real multiplications that were used in the polar raster reconstruction of Fig. 8(b). Fig. 9(a) displays poor image quality for the CGSS scheme reconstructions. Although the average sampling period of the CGSS scheme is just about as close to the polar raster sampling period as the other examples, the image quality for the CGSS scheme is noticeably worse. Once the sampling period becomes large for certain projections, and the adjacent samples become highly uncorrelated, severe interpolation errors will result. Thus, for the CGSS scheme, the deviation of the sampling period length from the average can introduce high error terms into (26), while the regular measurement geometry can avoid these sporadic high error terms by keeping the sampling period constant.

Figs. 10–14 present a comparison between the profiles of four different rows of the various reconstructed images (heavy line) and the actual image (thin line). The profiles reconstructed by the polar raster with linear interpolation reproduce the corners more distinctly than the CGSS scheme, especially for pixels near the center of the image. This was observed in the photographs of the reconstructions for features 5, 6, and 7. Some edges were reproduced better using the CGSS scheme as seen near position 1 of Fig. 10 and position 2 of Fig. 13.

The results presented here demonstrate the effects of the CGSS scheme on the efficiency of the filtered-backprojection algorithm for parallel-beam projections. For densely sampled objects, the CGSS scheme reduces the computational load with no apparent loss in image quality. Some features were reproduced more distinctly from the algorithm using the CGSS scheme while other features were not, but overall a comparable image quality existed between the two algorithms.

V. CONCLUSION

In this paper a scanning and sampling scheme was presented that in theory eliminates the calculations and errors associated with interpolation. Two relationships were derived to indicate the set of all possible projection angles and their corresponding sampling rates that yield an interpolation-free condition. A more practical modification was also presented, which placed upper and lower bounds

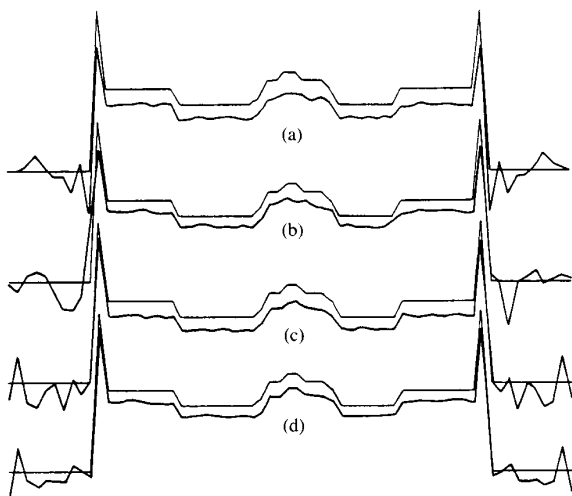


Fig. 11. Profiles for the same reconstructions used in Fig. 10 for row 28 of the images.

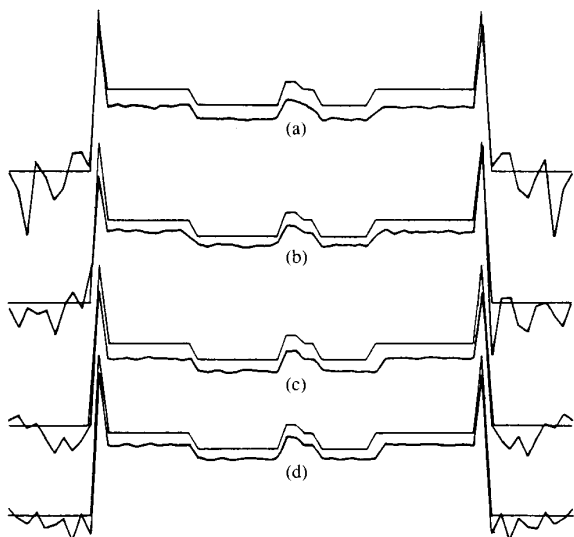


Fig. 12. Profiles of the same reconstructions used in Fig. 10 for row 36 of the images.

on the projection sampling rates. This modification resulted in the necessity for limited interpolation in the reconstruction of the image.

A loss in efficiency for the CGSS scheme was indicated for increasing pixel dimension and required number of projections, which suggests the limitation of the CGSS scheme's application to images of smaller pixel dimension. The simulations demonstrated that if the upper bounds on the sampling rate were too low, the conventional polar raster with interpolation produced superior results. Thus, the application of the CGSS scheme at lower sampling rates, relative to the Cartesian grid, is also limited. But, when higher sampling rates were used, the CGSS scheme resulted in a greater efficiency than the polar raster of regular measurement geometry at comparable image quality.

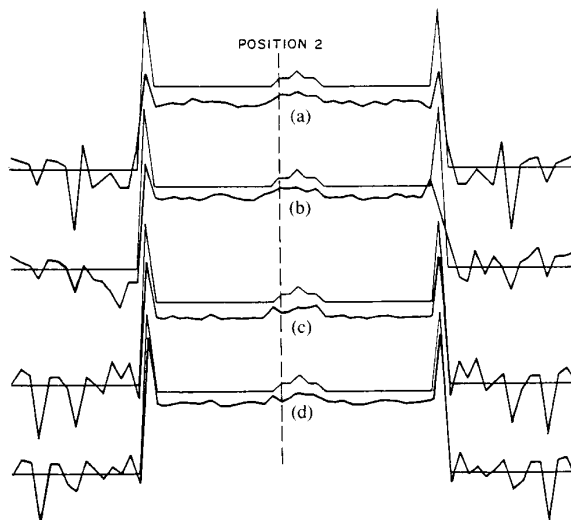


Fig. 13. Profiles for the same reconstructions used in Fig. 10 for row 52 of the images.

APPENDIX A

In this appendix, an analysis of the error due to *linear interpolation* and *numerical integration* (rectangular formula) on the filtered-projection data is examined. In this analysis, the ensemble of all possible filtered-projection functions are assumed wide sense stationary (WSS). The mean and the mean square error are derived in terms of the autocorrelation function $R(\tau)$.

Linear Interpolation

Consider the estimation of $Q(\xi_i)$ by linear interpolation from the values $Q(n\tau)$ and $Q((n-1)\tau)$, where τ is the sampling interval and $(n-1)\tau \leq \xi_i \leq n\tau$. The formula for the estimate of $Q(\xi_i)$ in this case is

$$\hat{Q}(\xi_i) = aQ(n\tau) + (1-a)Q((n-1)\tau) \quad (\text{A.1})$$

where $a = (\xi_i - (n-1)\tau)/\tau$ and $0 \leq a \leq 1$. Let e_{LI} denote the error resulting from linear interpolation; then the expected value or mean of the error is

$$\begin{aligned} E\{e_{LI}(a)\} &= E\{Q(\xi_i)\} - E\{Q((n-1)\tau)\} \\ &\quad + a(E\{Q((n-1)\tau)\} - E\{Q(n\tau)\}). \end{aligned} \quad (\text{A.2})$$

If $Q(t)$ is WSS then

$$E\{e_{LI}(a)\} = 0. \quad (\text{A.3})$$

The mean square error is given by

$$\begin{aligned} E\{e_{LI}^2(a)\} &= 2(\sigma_Q^2 + a(a-1) - aR((a-1)\tau)) \\ &\quad + a(1-a)R(\tau) - (1-a)R(a\tau) \end{aligned} \quad (\text{A.4})$$

where $R(\tau)$ is the autocorrelation function and σ_Q^2 is the variance of $Q(t)$ ($R(0) = \sigma_Q^2$). Equation (A.4) gives the mean square error as a function of the parameter a . If a

is assumed independent of $Q(t)$ and uniformly distributed over the interval $[0, 1]$, then (A.4) can be written as

$$E\{e_{LJ}^2\} = \frac{1}{3} \left[5\sigma_Q^2 + R(\tau) - 6 \int_0^1 \left\{ aR((a-1)\tau) - (a-1)R(a\tau) \right\} da \right]. \quad (\text{A.5})$$

From (A.5) it is observed that as the interval of interpolation (τ) approaches zero, the mean square error also approaches zero. Also, for increasing correlation of the function $Q(t)$ over the interval of interpolation (i.e., the values of $R(t)$ for $|t| \leq \tau$ approach σ_Q^2), the error approaches zero.

Numeric Integration

Consider the estimate of the integral F given as

$$F = \int_a^b Q(\theta) d\theta \quad (\text{A.6})$$

by numeric integration using the rectangular formula

$$\hat{F} = \sum_{i=1}^N Q(\theta_i) \Delta\theta_i \quad (\text{A.7})$$

where the set of all $\Delta\theta_i$ are the lengths of a set of subintervals that partition the interval $[a, b]$, and θ_i is some point in the i th subinterval. The error in this estimate can be written as

$$e_{RF}(\bar{\theta}, \bar{\Delta\theta}) = \int_a^b Q(\theta) d\theta - \sum_{i=1}^N Q(\theta_i) \Delta\theta_i \quad (\text{A.8})$$

where the error is a function of all θ_i 's and $\Delta\theta_i$'s given as elements of the vectors $\bar{\theta}$ and $\bar{\Delta\theta}$, respectively. If the integral over the interval $[a, b]$ is broken into N integrals corresponding to the subintervals of the numeric integration, then (A.8) can be written as

$$e_{RF}(\bar{\theta}, \bar{\Delta\theta}) = \sum_{i=1}^N \left\{ \frac{1}{\Delta\theta_i} \int_{\Delta\theta_i} Q(\theta) d\theta - Q(\theta_i) \right\} \Delta\theta_i. \quad (\text{A.9})$$

By the theorem of the mean for integrals, if $Q(t)$ is continuous in the i th interval then there exists a point ξ_i in the i th interval such that

$$\frac{1}{\Delta\theta_i} \int_{\Delta\theta_i} Q(\theta) d\theta = Q(\xi_i). \quad (\text{A.10})$$

The point, ξ_i , can be considered the optimal choice for a sample value in the interval that minimizes the error in numeric integration. Equation (A.9) can now be written as

$$e_{RF}(\bar{\theta}, \bar{\Delta\theta}) = \sum_{i=1}^N \left\{ Q(\xi_i) - Q(\theta_i) \right\} \Delta\theta_i. \quad (\text{A.11})$$

If $Q(t)$ is WSS then the mean of the error is

$$E\{e_{RF}\} = 0 \quad (\text{A.12})$$

and the mean square error is

$$\begin{aligned} E\{e_{RF}^2(\bar{\theta}, \bar{\Delta\theta})\} &= 2 \sum_{i=1}^N \left\{ \sigma_Q^2 - R(\theta_i - \xi_i) \right\} \Delta\theta_i^2 \\ &+ 2 \sum_{i=1}^N \sum_{j=i+1}^N \left\{ R(\xi_i - \xi_j) - R(\theta_j - \xi_i) \right. \\ &\quad \left. - R(\theta_i - \xi_j) + R(\theta_i - \theta_j) \right\} \Delta\theta_i \Delta\theta_j. \end{aligned} \quad (\text{A.13})$$

The cross-product terms in the double summation represent the correlation between the intervals of the integration, while the single summation represents the correlation within the same interval. Equation (A.13) can be used as a basis to determine $\bar{\Delta\theta}$ and $\bar{\theta}$ so that the mean square error is minimized. The choice of $\bar{\Delta\theta}$ is dependent on the expected value of error for each subinterval which is represented by the individual terms of the first summation in (A.13). In the intervals where the error is expected high [low correlation of $Q(\theta)$], the interval should be made small. Since it was assumed that the functions were WSS, the autocorrelation function is independent of any particular point t . It is only dependent on the distance between the points. Therefore, since no *a priori* information is available to indicate where the specific regions of high and low correlation exist, all the $\Delta\theta_i$'s should be chosen equal.

The knowledge of the exact locations of the points ξ_i is not available. Therefore, the various locations of these points within the intervals can be modeled by a probability density function $p_{\xi_i}(\xi_i)$. The minimization of the mean square error in (A.13), without explicit knowledge of $R(\tau)$, can be approached by determining θ_i to minimize the average deviation from ξ_i . This only assumes that the autocorrelation function is uniformly continuous and that $R(\tau)$ approaches σ_Q^2 as τ approaches zero. The average deviation of θ_i from ξ_i is given by

$$E\{(\theta_i - \xi_i)^2\} = \int_{\Delta\theta_i} (\theta_i - \xi_i)^2 p_{\xi_i}(\xi_i) d\xi_i. \quad (\text{A.14})$$

The result for optimal θ_i given $p_{\xi_i}(\xi_i)$ is

$$\theta_i = E\{\xi_i\}. \quad (\text{A.15})$$

In typical situations $p_{\xi_i}(\xi)$ can be assumed symmetric about the center of the interval (as in the case when no *a priori* knowledge is available and the uniform distribution is assumed), then the midpoint of that interval would be the best choice.

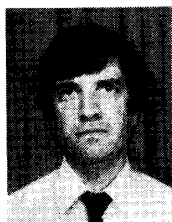
Therefore, to minimize the arguments of the autocorrelation functions in (A.13), and thereby minimize mean square error, θ_i must be chosen equal to $E\{\xi_i\}$. In the case of a symmetrical distribution for ξ_i , $E\{\xi_i\}$ is the midpoint. If complete freedom to choose θ_i is not present, choose θ_i close to $E\{\xi_i\}$. Finally, if the explicit expressions for $R(t)$, $p_{\xi_i}(\xi_i)$, and $p_{\theta_i}(\theta_i)$ are known, then the mean square error is obtained via (A.13).

ACKNOWLEDGMENT

The authors would like to thank the anonymous reviewers for their efforts and helpful comments that contributed to the improvement of this manuscript.

REFERENCES

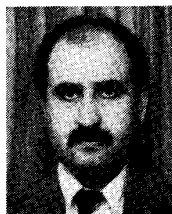
- [1] A. C. Kak, "Image reconstruction from projections," in *Notes on Image Processing: Restoration, Compression and Reconstruction from Projections*, Purdue Univ., Dec. 1980.
- [2] L. Wang "Cross-section reconstruction with a fan-beam scanning geometry," *IEEE Trans. Comput.*, vol. C-26, pp. 264-268, Mar. 1977.
- [3] A. V. Lakshminarayanan, "Reconstruction from divergent ray data," Dept. Comput. Sci., State Univ. New York at Buffalo, Tech. Rep. 92, 1975.
- [4] D. Nahamoo, C. R. Crawford, and A. C. Kak, "Design constraints and reconstruction algorithms for traverse-continuous-rotate CT scanners," *IEEE Trans. Biomed. Eng.*, vol. BME-28, pp. 79-98, Feb. 1981.
- [5] B. D. Smith, "Derivation of the extended fan-beam formula," *IEEE Trans. Med. Imaging*, vol. MI-4, pp. 177-184, Dec. 1985.
- [6] G. T. Gullberg, C. R. Crawford, and B. M. W. Tsui, "Reconstruction algorithm for fan-beam with a displaced center-of-rotation," *IEEE Trans. Med. Imaging*, vol. MI-5, pp. 23-29, Mar. 1986.
- [7] R. M. Mersereau and A. V. Oppenheim, "Digital reconstruction of multidimensional signals from their projections," *Proc. IEEE*, vol. 62, pp. 1319-1338, Oct. 1974.
- [8] K. D. Donohue and J. Saniie, "Interpolation-free scanning and sampling scheme for tomographic reconstructions," in *Medical Imaging*, R. H. Schneider and S. J. Dwyer III, Eds., *Proc. SPIE 767*, Feb. 1987, pp. 62-69.
- [9] C. R. Crawford and A. C. Kak, "Aliasing artifacts in computerized tomography," *Appl. Opt.*, vol. 18, pp. 3704-3711, 1979.
- [10] L. A. Shepp and B. F. Logan, "The Fourier reconstruction of a head section," *IEEE Trans Nucl. Sci.*, vol. NS-21, pp. 21-43, 1974.
- [11] N. C. Gallagher, Jr., and G. L. Wise, "A theoretical analysis of properties of median filters," *IEEE Trans. Acoust., Speech, Signal Processing*, vol. ASSP-29, pp. 1136-1141, Dec. 1981.



Kevin D. Donohue (S'84-M'87) was born in Chicago, IL, on April 19, 1958. He received the B.A. degree in mathematics from Northeastern Illinois University in 1981. He received the B.S., M.S., and Ph.D. degrees in electrical engineering from Illinois Institute of Technology in 1984, 1985, and 1987, respectively.

He worked at Zenith Electronics in Glenview, IL, in 1985, developing ultrasonic detection circuits. He is currently an Assistant Professor in the Electrical and Computer Engineering Department at Drexel University in Philadelphia, PA. His current research interests include radar and ultrasonic detection systems, detection and estimation theory, statistical pattern recognition, image processing, and information processing.

Dr. Donohue is a member of SPIE.



Jafar Saniie (S'80-M'81) was born in Iran on March 21, 1952. He received the B.S. degree in electrical engineering from the University of Maryland in 1974. In 1977 he received the M.S. degree in biomedical engineering from Case Western Reserve University and, in 1981, the Ph.D. degree in electrical engineering from Purdue University.

In 1981 he joined the Applied Physics Laboratory, University of Helsinki, Finland, to conduct research in photothermal and photoacoustic imaging. Since 1983 he has been with the Department of Electrical and Computer Engineering, Illinois Institute of Technology, where he is an Associate Professor and Director of the Ultrasonic Information Processing Laboratory. His current research activities include radar signal processing, estimation and detection, ultrasonic medical imaging, computer tomography, nondestructive testing, and digital hardware design.

Dr. Saniie is a member of the American Society for Engineering, Sigma Xi, Tau Beta Pi, Eta Kappa Nu, and has been IEEE Student Branch Counselor since 1983. He is the 1986 recipient of the Outstanding IEEE Student Counselor Award.